Supporting Information

Model Order Reduction of Large-scale Metasurfaces using a Hierarchical Dipole Approximation

Mohammad Mahdi Salary[1], *Ali Forouzmand*[1] *and Hossein Mosallaei*[1*]

[1]Department of Electrical and Computer Engineering, Northeastern University, Boston,

Massachusetts 02115, United States

[*]hossseinm@ece.neu.edu

The purpose of this document is to provide more details regarding the formulation and technical implementation of the method as well as providing the retrieved polarizability data for all the elements. The document is organized as follows. In the first section, we provide the expressions for free space dyadic Green's functions. In the second section 3D periodic dyadic Green's functions over 2D infinite arrays are derived and the performance of Ewald's acceleration technique is evaluated. The third section discusses the applicability of discrete complex image method (DCIM) for evaluating dyadic Green's functions of electric and magnetic dipoles above substrates. The $\mathcal{H}$ -matrix representation of the system of equations is briefed in section 4. Finally, section 5 provides the data of the retrieved polarizabilities corresponding to the elements studied in the paper. Throughout this work, we assume a time convention of $\exp(-i\omega t)$.

1- Dyadic Green's Functions

In this section, we provide the expressions for the free-space dyadic Green's functions. All the dyadic Green's functions can be expressed in terms of principal diagonal and anti-diagonal Green's tensors as:

$$\hat{G}^{EP}(\bar{r}_j,\bar{r}_l)=\frac{k_0^2}{\varepsilon_0}\hat{G}^{pd}(\bar{r}_j,\bar{r}_l) \tag{S1}$$

$$\hat{G}^{EM}(\bar{r}_j,\bar{r}_l)=i\omega\mu\hat{G}^{ad}(\bar{r}_j,\bar{r}_l) \tag{S2}$$

$$\hat{G}^{HP}(\bar{r}_j,\bar{r}_l)=-i\omega\hat{G}^{ad}(\bar{r}_j,\bar{r}_l) \tag{S3}$$

$$\hat{G}^{HM}(\bar{r}_j,\bar{r}_l)=k_0^2\hat{G}^{pd}(\bar{r}_j,\bar{r}_l) \tag{S4}$$

where the principal diagonal $\hat{G}^{pd}(\bar{r}_j,\bar{r}_l)$ and anti-diagonal $\hat{G}^{ad}(\bar{r}_j,\bar{r}_l)$ Green's tensors are related to the scalar free-space Green's function $g(\bar{r}_j,\bar{r}_l)=e^{ik_0|\bar{r}_j-\bar{r}_l|}/4\pi\left|\bar{r}_j-\bar{r}_l\right|$ as:

$$\hat{G}^{pd}(\bar{r}_j,\bar{r}_l)=g(\bar{r}_j,\bar{r}_l)\hat{I}+\frac{1}{k_0^2}\nabla\nabla g(\bar{r}_j,\bar{r}_l)$$
$$=\left\{\left(\frac{3}{k_0^2\left|\bar{r}_j-\bar{r}_l\right|^2}-\frac{3i}{k_0\left|\bar{r}_j-\bar{r}_l\right|}-1\right)\frac{\left(\bar{r}_j-\bar{r}_l\right)\otimes\left(\bar{r}_j-\bar{r}_l\right)}{\left|\bar{r}_j-\bar{r}_l\right|^2}+\left(1+\frac{i}{k_0\left|\bar{r}_j-\bar{r}_l\right|}-\frac{1}{k_0^2\left|\bar{r}_j-\bar{r}_l\right|^2}\right)\hat{I}\right\}g(\bar{r}_j,\bar{r}_l) \tag{S5}$$

$$\hat{G}^{ad}(\bar{r}_j,\bar{r}_l)=\nabla g(\bar{r}_j,\bar{r}_l)\times\hat{I}=\left(ik_0-\frac{1}{\left|\bar{r}_j-\bar{r}_l\right|}\right)g(\bar{r}_j,\bar{r}_l)\frac{\bar{r}_j-\bar{r}_l}{\left|\bar{r}_j-\bar{r}_l\right|}\times\hat{I} \tag{S6}$$

In the above equations $k_0=\omega/c$ is the wavenumber with ω and c being the angular frequency and speed of light, respectively, $\hat{I}$ is the unit dyad and $\otimes$ denotes dyadic product.

2- Periodic Green's Functions: Ewald Acceleration Method

This section is focused on the evaluation of periodic dyadic Green's functions in DDA. In [1], the efficient evaluation of these function is explained for 3D periodic arrays through the use of Ewald's acceleration technique [2-4]. Here, we have implemented 3D Periodic Green's Function over 2D periodic arrays as needed for design purposes in metasurfaces.

Consider a periodic lattice placed in the x-y plane with periods d_x and d_y along x- and y- axes as shown in Figure S1. The 3D Periodic Scalar Green's Function in a homogeneous media for such a 2D periodicity in free space for a wavevector $\bar{k}_0=\left(k_{0x},\quad k_{0y},\quad k_{0z}\right)$ is expressed by:

$$g_\infty(\bar{r})=\frac{1}{4\pi}\sum_{n=-\infty}^{+\infty}\sum_{m=-\infty}^{+\infty}\frac{e^{ik_0R_{nm}}}{R_{nm}}e^{i\bar{\beta}_0\cdot\bar{\rho}_{nm}} \tag{S7}$$

where :

$$\bar{\rho}_{nm}=\left(nd_x,\quad md_y,\quad 0\right) \tag{S8}$$

$$\bar{R}_{nm}=\bar{r}-\bar{\rho}_{nm} \tag{S9}$$

$$\bar{\beta}_0=\left(k_{0x},\quad k_{0y},\quad 0\right) \tag{S10}$$

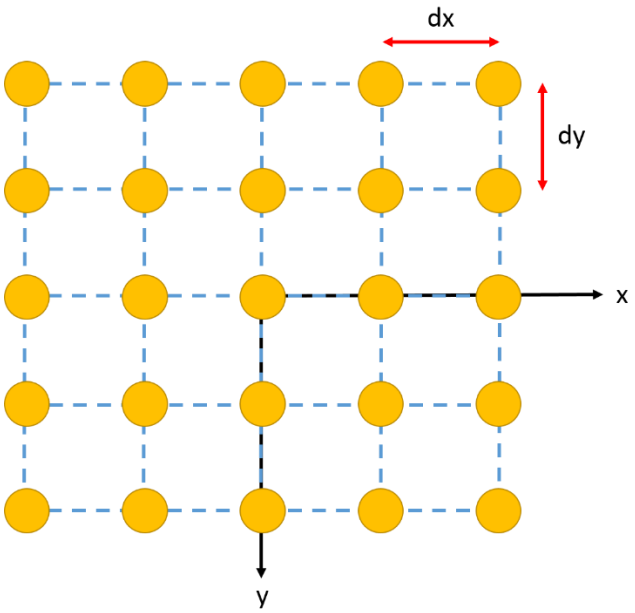

Figure S1. The schematic representation of a 2D periodic lattice.

The principal diagonal and anti-diagonal Green's tensors can be subsequently obtained as:

$$\hat{G}_{\infty}^{pd}(\bar{r}) = g_{\infty}(\bar{r}_j, \bar{r}_l)\hat{I} + \frac{1}{k_0^2}\nabla\nabla g_{\infty}(\bar{r}_j, \bar{r}_l) \tag{S11}$$

$$\hat{G}_{\infty}^{ad}(\bar{r}_j, \bar{r}_l) = \nabla g_{\infty}(\bar{r}_j, \bar{r}_l) \times \hat{I} \tag{S12}$$

which lead to:

$$\hat{G}_{\infty}^{pd}(\bar{r}) = \frac{1}{4\pi}\sum_{n=-\infty}^{+\infty}\sum_{m=-\infty}^{+\infty}\left\{\left(\frac{3}{k_0^2 R_{nm}^{\ 2}} - \frac{3i}{k_0 R_{nm}} - 1\right)\frac{\bar{R}_{nm} \otimes \bar{R}_{nm}}{R_{nm}^{\ 2}} + \left(1 + \frac{i}{k_0 R_{nm}} - \frac{1}{k_0^2 R_{nm}^{\ 2}}\right)\hat{I}\right\}\frac{e^{ik_0 R_{nm}}}{R_{nm}} e^{i\bar{\beta}_0 \cdot \bar{\rho}_{nm}} \tag{S13}$$

$$\hat{G}_{\infty}^{ad}(\bar{r}) = \frac{1}{4\pi}\sum_{n=-\infty}^{+\infty}\sum_{m=-\infty}^{+\infty}\left(ik_0 - \frac{1}{R_{nm}}\right)\frac{\bar{R}_{nm}}{R_{nm}} \times \hat{I}\,\frac{e^{ik_0 R_{nm}}}{R_{nm}} e^{i\bar{\beta}_0 \cdot \bar{\rho}_{nm}} \tag{S14}$$

In the above equations $\hat{I}$ is the unit dyad and $\otimes$ stands for dyadic product. Equations (S13) and (S14) lead to series with a poor convergence $O(1/N)$, making the calculations prohibitive as they require a large number of terms to converge.

In the Ewald representation [2] the scalar Green's function in (S7) is decomposed into the hybrid sum of spectral and spatial scalar terms, as:

$$g_{\infty}(\bar{r}) = g_{\infty}^{spectral}(\bar{r}) + g_{\infty}^{spatial}(\bar{r}) \tag{S15}$$

where:

$$g_{\infty}^{spectral}(\bar{r}) = -\frac{1}{4id_x d_y}\sum_{n=-\infty}^{+\infty}\sum_{m=-\infty}^{+\infty}\frac{e^{i\bar{k}_t(n,m).\bar{r}}}{k_z(n,m)}\times\sum_{\pm}e^{\pm izk_z(n,m)}\,\mathrm{erfc}\left[\frac{-ikz_z(n,m)}{2E}\mp zE\right] \tag{S16}$$

$$g_{\infty}^{spatial}(\bar{r}) = \frac{1}{8\pi}\sum_{n=-\infty}^{+\infty}\sum_{m=-\infty}^{+\infty}\frac{e^{ik_0\rho_{nm}}}{R_{nm}}\times\sum_{\pm}e^{\pm ik_0R_{nm}}\,\mathrm{erfc}\left[R_{nm}E\pm i\frac{k_0}{2E}\right] \tag{S17}$$

with $\bar{k}_t(n,m) = \left(k_x + 2n\pi/d_x,\quad k_y + 2m\pi/d_y,\quad 0\right)$ and $k_z(n,m) = \sqrt{k_0^2 - k_t(n,m)^2}$.

The adopted Ewald parameter E is:

$$E = E_{opt} = \sqrt{\frac{\pi}{d_x d_y}} \tag{S18}$$

which is chosen to minimize the total number of terms required for a given accuracy, since with this choice both spectral and spatial terms exhibit the same Gaussian convergence rate [4].

It should be noted that a singular point is present in the spatial term when $R_{nm}\to 0$. This singularity can be removed by regularizing the Green's function and taking the limit $R_{nm}\to 0$. However, this singular point will not be treated in our formulation because it is irrelevant for DDA where the self-interactions are described through polarizabilities.

In order to obtain the expression for the principal diagonal and anti-diagonal Green's functions using (S10) and (S11), we have:

$$\nabla g_{\infty}^{spectral}(\bar{r}) = -\frac{1}{4d_x d_y}\sum_{n=-\infty}^{+\infty}\sum_{m=-\infty}^{+\infty}\bar{k}_t(n,m)\frac{e^{i\bar{k}_t(n,m).\bar{r}}}{k_z(n,m)}\times\sum_{\pm}e^{\pm izk_z(n,m)}\,\mathrm{erfc}\left[\frac{-ik_0z_z(n,m)}{2E}\mp zE\right] \tag{S19}$$

$$\nabla g_{\infty}^{spatial}(\bar{r}) = \frac{1}{8\pi}\sum_{n=-\infty}^{+\infty}\sum_{m=-\infty}^{+\infty}e^{ik_0\rho_{nm}}\left(\frac{f'(R_{nm})}{R_{nm}} - \frac{f(R_{nm})}{R_{nm}^{\,2}}\right)\frac{\bar{R}_{nm}}{R_{nm}} \tag{S20}$$

$$\nabla\nabla g_{\infty}^{spectral}(\bar{r}) = \frac{1}{4id_x d_y}\sum_{n=-\infty}^{+\infty}\sum_{m=-\infty}^{+\infty}\bar{k}_t(n,m)\otimes\bar{k}_t(n,m)\frac{e^{i\bar{k}_t(n,m).\bar{r}}}{k_z(n,m)}\times\sum_{\pm}e^{\pm izk_z(n,m)}\,\mathrm{erfc}\left[\frac{-ik_0z_z(n,m)}{2E}\mp zE\right] \tag{S21}$$

$$\nabla\nabla g_{\infty}^{spatial}(\bar{r}) = \frac{1}{8\pi}\sum_{n=-\infty}^{+\infty}\sum_{m=-\infty}^{+\infty}\begin{array}{l} e^{ik_0\rho_{nm}}\left(\dfrac{f'(R_{nm})}{R_{nm}^{\,2}} - \dfrac{f(R_{nm})}{R_{nm}^{\,3}}\right)\hat{I} \\ +e^{ik_0\rho_{nm}}\left(\dfrac{f''(R_{nm})}{R_{nm}} - \dfrac{3f'(R_{nm})}{R_{nm}^{\,2}} + \dfrac{3(R_{nm})}{R_{nm}^{\,3}}\right)\dfrac{\bar{R}_{nm}\otimes\bar{R}_{nm}}{R_{nm}^{\,2}}\end{array} \tag{S22}$$

in which:

$$f(R_{nm}) = \sum_{\pm} e^{\pm ik_0 R_{nm}} \operatorname{erfc}\left[R_{nm}E \pm i\frac{k_0}{2E} \right] \tag{S23}$$

$$f'(R_{nm}) = ik_0 \sum_{\pm} \pm e^{ik_0 R_{nm}} \operatorname{erfc}\left[R_{nm}E \pm i\frac{k_0}{2E} \right] - \frac{2E}{\sqrt{\pi}} \sum_{\pm} e^{-(R_{nm}E \pm i\frac{k_0}{2E})^2} e^{\pm ik_0 R_{nm}} \tag{S24}$$

$$f''(R_{nm}) = -k_0^2 f(R_{nm}) + \frac{4ik_0 E}{\sqrt{\pi}} \sum_{\pm} e^{-\left(R_{nm}E \pm i\frac{k_0}{2E}\right)^2 \pm ik_0 R_{nm}} + \frac{4E^2}{\sqrt{\pi}} \sum_{\pm} \left(R_{nm}E \pm i\frac{k_0}{2E} \right) e^{-\left(R_{nm}E \pm i\frac{k_0}{2E}\right)^2 \pm ik_0 R_{nm}} \tag{S25}$$

The expressions obtained with Ewald method have a Gaussian convergence rate, so only a handful of summation terms are needed to achieve convergence. Figure S2 compares the convergence of principal diagonal Green's function through regular summation with a truncation number of $N = 100$ and by applying Ewald acceleration technique with a truncation number of $N = 2$ corresponding to the case of $k_0 d_x = k_0 d_y = 1$, $k_{0x} = k_{0y} = 0$ and $z = 2d_x = 2d_y$. As it can be seen, while the regular summation has a poor convergence and requires a very large number of terms, the Ewald's method quickly converges with a high numerical accuracy. As it has been shown in [1], all the dyadic Green's functions have the same convergence rate and a maximal truncation number of $N = 2$ is required.

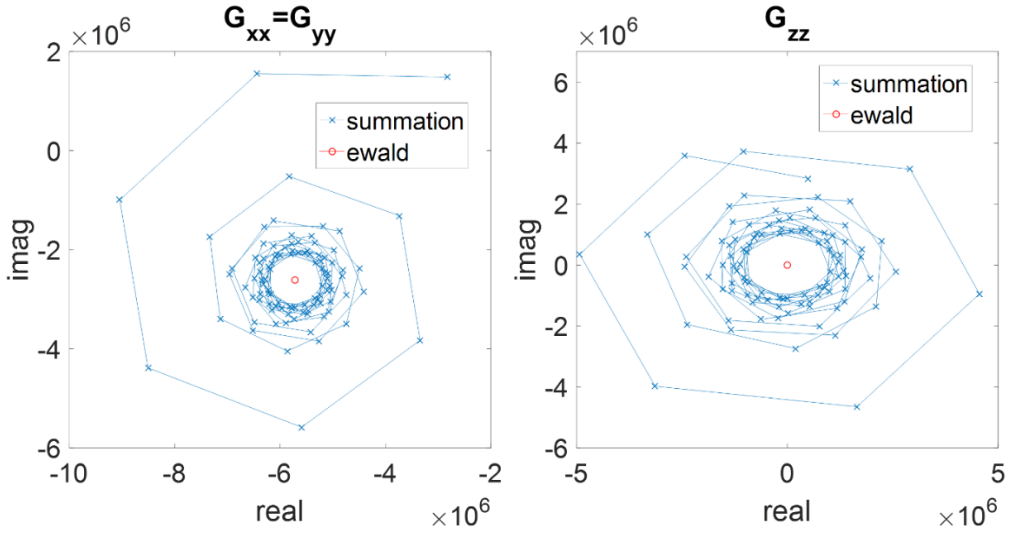

Figure S2. Comparison of the convergence of principal diagonal Green's function through regular summation with a truncation number of N=100 and applying Ewald acceleration technique with a truncation number of N=2, corresponding to the case of $k_0 d_x = k_0 d_y = 1$, $k_{0x} = k_{0y} = 0$ and $z = 2d_x = 2d_y$.

3- Discrete Complex Image Method (DCIM):

Compared to the IE-based approaches relying on free-space Green's function and DE-based methods, the modeling complexity in dealing with certain type of geometries such as a semi-infinite substrate, or a multilayer substrate can be greatly reduced in DDA by incorporating the Dyadic Green's functions of layered media. The DDA formulation used in this work incorporates the Green's function of layered media which enables us to take into account the scattering effect

of the substrate without the necessity of discretization. This makes it possible to model larger problems involving wave propagation in layered media. We express the substrate contribution to the scattering as follows:

$$\hat{G}_S(\bar{r}_j,\bar{r}_l)=\begin{bmatrix}\hat{G}_S^{EP}(\bar{r}_j,\bar{r}_l) & \hat{G}_S^{HM}(\bar{r}_j,\bar{r}_l)\\ \hat{G}_S^{HP}(\bar{r}_j,\bar{r}_l) & \hat{G}_S^{HM}(\bar{r}_j,\bar{r}_l)\end{bmatrix} \tag{S26}$$

where $G_S^{EP}(\bar{r}_j,\bar{r}_l)$, $G_S^{EM}(\bar{r}_j,\bar{r}_l)$, $G_S^{HP}(\bar{r}_j,\bar{r}_l)$ and $G_S^{HM}(\bar{r}_j,\bar{r}_l)$ are the Green's tensor expressed in terms of Sommerfeld integrals as [5]:

$$\hat{G}_S^{EP}(\bar{r}_j,\bar{r}_l)=\frac{i}{8\pi\varepsilon_0}\begin{pmatrix}k_0^2+\frac{\partial^2}{\partial x^2} & \frac{\partial^2}{\partial x\partial y} & \frac{\partial^2}{\partial x\partial z}\\ \frac{\partial^2}{\partial y\partial x} & k_0^2+\frac{\partial^2}{\partial y^2} & \frac{\partial^2}{\partial y\partial z}\\ \frac{\partial^2}{\partial z\partial x} & \frac{\partial^2}{\partial z\partial y} & k_0^2+\frac{\partial^2}{\partial z^2}\end{pmatrix}\begin{pmatrix}-\int_{-\infty}^{+\infty}dk_\rho\frac{k_\rho}{k_z}H_0^{(1)}(k_\rho\rho)R^{TM}\left(k_z\right)e^{ik_z(z_l-z_j+2d)}\\ \int_{-\infty}^{+\infty}dk_\rho\frac{k_\rho}{k_z}H_0^{(1)}(k_\rho\rho)R^{TE}\left(k_z\right)e^{ik_z(z_l-z_j+2d)}\\ \int_{-\infty}^{+\infty}dk_\rho\frac{k_\rho}{k_z}H_0^{(1)}(k_\rho\rho)R^{TM}\left(k_z\right)e^{ik_z(z_l-z_j+2d)}\end{pmatrix} \tag{S27}$$

$$\hat{G}_S^{HP}(\bar{r}_j,\bar{r}_l)=\frac{i\omega\mu}{8\pi}\begin{pmatrix}0 & -\frac{\partial}{\partial z} & \frac{\partial}{\partial y}\\ \frac{\partial}{\partial z} & 0 & -\frac{\partial}{\partial x}\\ -\frac{\partial}{\partial y} & \frac{\partial}{\partial x} & 0\end{pmatrix}\begin{pmatrix}-\int_{-\infty}^{+\infty}dk_\rho\frac{k_\rho}{k_z}H_0^{(1)}(k_\rho\rho)R^{TE}\left(k_z\right)e^{ik_z(z_l-z_j+2d)}\\ \int_{-\infty}^{+\infty}dk_\rho\frac{k_\rho}{k_z}H_0^{(1)}(k_\rho\rho)R^{TM}\left(k_z\right)e^{ik_z(z_l-z_j+2d)}\\ \int_{-\infty}^{+\infty}dk_\rho\frac{k_\rho}{k_z}H_0^{(1)}(k_\rho\rho)R^{TE}\left(k_z\right)e^{ik_z(z_l-z_j+2d)}\end{pmatrix} \tag{S28}$$

where *d* is the distance between the source and the substrate interface as shown in Figure S3. And simply by applying duality, we obtain:

$$\hat{G}_S^{HM}(\bar{r}_j,\bar{r}_l)=\frac{i}{8\pi}\begin{pmatrix}k^2+\frac{\partial^2}{\partial x^2} & \frac{\partial^2}{\partial x\partial y} & \frac{\partial^2}{\partial x\partial z}\\ \frac{\partial^2}{\partial y\partial x} & k^2+\frac{\partial^2}{\partial y^2} & \frac{\partial^2}{\partial y\partial z}\\ \frac{\partial^2}{\partial z\partial x} & \frac{\partial^2}{\partial z\partial y} & k^2+\frac{\partial^2}{\partial z^2}\end{pmatrix}\begin{pmatrix}-\int_{-\infty}^{+\infty}dk_\rho\frac{k_\rho}{k_z}H_0^{(1)}(k_\rho\rho)R^{TM}\left(k_z\right)e^{ik_z(z_l-z_j+2d)}\\ \int_{-\infty}^{+\infty}dk_\rho\frac{k_\rho}{k_z}H_0^{(1)}(k_\rho\rho)R^{TE}\left(k_z\right)e^{ik_z(z_l-z_j+2d)}\\ \int_{-\infty}^{+\infty}dk_\rho\frac{k_\rho}{k_z}H_0^{(1)}(k_\rho\rho)R^{TM}\left(k_z\right)e^{ik_z(z_l-z_j+2d)}\end{pmatrix} \tag{S29}$$

$$\hat{G}_S^{EM}(\bar{r}_j,\bar{r}_l)=\frac{-i\omega}{8\pi}\begin{pmatrix}0 & -\frac{\partial}{\partial z} & \frac{\partial}{\partial y}\\ \frac{\partial}{\partial z} & 0 & -\frac{\partial}{\partial x}\\ -\frac{\partial}{\partial y} & \frac{\partial}{\partial x} & 0\end{pmatrix}\begin{pmatrix}-\int_{-\infty}^{+\infty}dk_\rho\frac{k_\rho}{k_z}H_0^{(1)}(k_\rho\rho)R^{TE}\left(k_z\right)e^{ik_z(z_l-z_j+2d)}\\ \int_{-\infty}^{+\infty}dk_\rho\frac{k_\rho}{k_z}H_0^{(1)}(k_\rho\rho)R^{TM}\left(k_z\right)e^{ik_z(z_l-z_j+2d)}\\ \int_{-\infty}^{+\infty}dk_\rho\frac{k_\rho}{k_z}H_0^{(1)}(k_\rho\rho)R^{TE}\left(k_z\right)e^{ik_z(z_l-z_j+2d)}\end{pmatrix} \tag{S30}$$

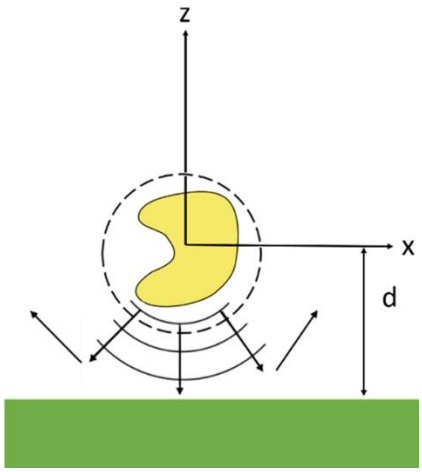

Figure S3. Schematic of a scatterer placed above a substrate.

The Sommerfeld integrals in Eqs. (S27) – (S30) have no analytic solution and the numerical integration strategy is very inefficient and time consuming as they are infinite, oscillatory and slowly convergent integrals. Here, we will apply the DCIM to accelerate the evaluation of Sommerfeld integrals [6, 7].

If the reflection coefficients can be approximated by a series of complex exponentials,

$$R^{TE,TM}\left(k_z\right)=\sum_{i=1}^{M_{TE,TM}}\alpha_i^{TE,TM}e^{k_z\beta_i^{TE,TM}} \tag{S31}$$

by utilizing the Sommerfeld identity [5],

$$\frac{e^{ik_0r}}{r}=i\int_0^\infty dk_\rho\frac{k_\rho}{k_{mz}}H_0(k_\rho\rho)e^{ik_z|z|},\quad r=\sqrt{\rho^2+z^2} \tag{S32}$$

the infinite integrals can be evaluated in a closed form as,

$$\int_{-\infty}^{+\infty}dk_\rho\frac{k_\rho}{k_z}H_0^{(1)}(k_\rho\rho)R^{TM,TE}e^{ik_z(z_l-z_j+2d)}=\sum_{i=1}^{M_{TE,TM}}\alpha_i^{TE,TM}\frac{e^{ikr_i^{TE,TM}}}{r_i^{TE,TM}},\quad r_i^{TE,TM}=\sqrt{\rho^2+\left(z_l-z_j+2d-i\beta_i^{TE,TM}\right)^2} \tag{S33}$$

The complex exponential series can be obtained from the modified Prony extrapolation technique. The details of the modified Prony method can be found elsewhere and is not repeated here [8, 9]. In order to have a good accuracy in the presence of surface wave poles (guided modes) or branch point singularity (lateral waves), we deform the sampling path as:

$$k_z = k_i\left[it + \left(1 - \frac{t}{T}\right)\right], \quad 0 \le t \le T \tag{S34}$$

Approximating the reflection coefficients in terms of the modified contour parameter (t):

$$R^{TE,TM}(t) = \sum_{i=1}^{M_{TE,TM}} A_i^{TE,TM} e^{tB_i^{TE,TM}} \tag{S35}$$

we can write:

$$\alpha_n = A_n \exp\left(\frac{TB_n}{1 - iT}\right); \quad \beta_n = -\frac{TB_n}{k(1 - iT)} \tag{S36}$$

Finally, the Green's tensors expressing the contribution of substrate can be written explicitly as a series of free-space dyadic Green's functions with complex distances and amplitudes and can be applied in both periodic and aperiodic cases. Therefore, the computation can be made to be the same order as the free space problems.

The accuracy of the solution directly depends on the approximation of the reflection coefficients. This relies on the choice of the truncation point (T), the number of images $M_{TE,TM}$ and the number of sample points $P_{TE,TM}$ in the modified Prony technique. The error values in spectral domain may cause high error in space domain for far zone fields. Therefore, it is necessary to consider choosing the parameters with high attention. Repetition and recursive iterations will ensure the choice of suitable values for a desired accuracy [10].

Generally, the required number of images and the truncation point increase with the local density of states in the substrate. In order to capture the guided modes contribution, one needs to employ multi-level schemes in DCIM [11]. In order to illustrate this, consider the silica half-space with $\varepsilon = 2.25$ at $\lambda = 10\mu m$. Since the substrate does not support any guided modes, the behavior of the reflection coefficient on the modified contour is smooth and can be extrapolated with a high accuracy by adopting $T = 8,\ N_{TE.TM} = 22,\ P_{TE.TM} = 12$. Figure S4 compares the exact and extrapolated reflection coefficient magnitude and phase for both TE and TM polarizations:

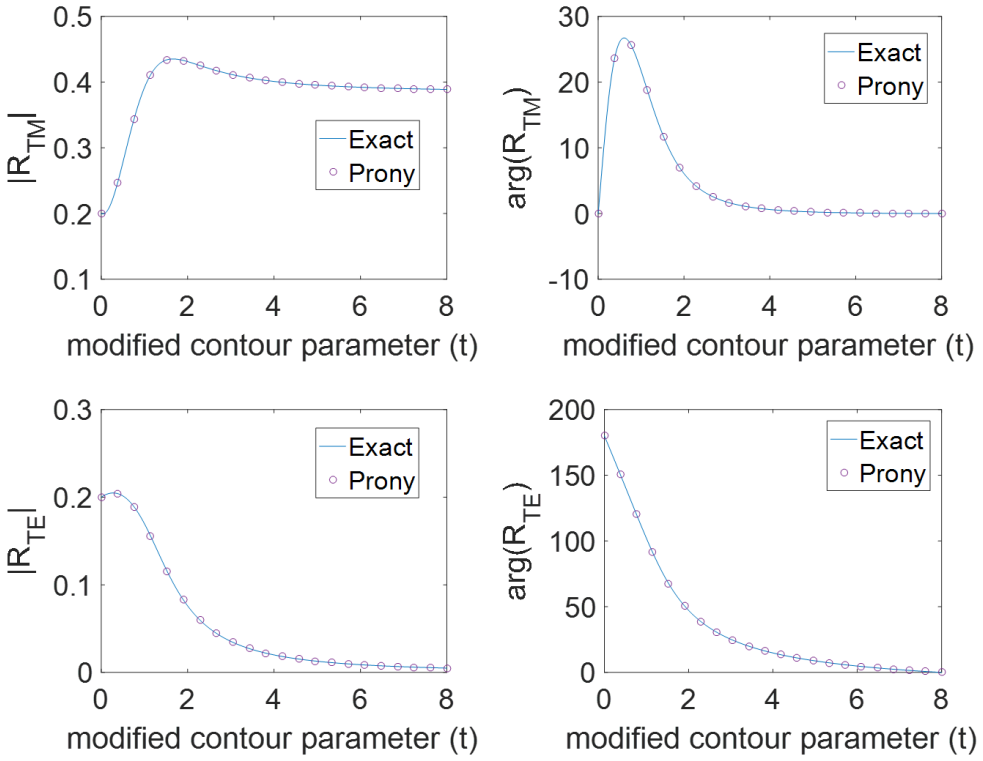

Figure S4. Comparison the exact and extrapolated reflection coefficient magnitude and phase for both TE and TM polarizations, corresponding to a silica substrate and by adopting $T=8,\ N_{TE.TM}=22,\ P_{TE.TM}=12$.

Now if we put a graphene layer with a doping level of $\mu_c=0.16ev$ and relaxation time $\tau_s=0.5ps$ of onto the substrate, the local density of states increases drastically and specifically one needs a very larger truncation point ($T=120$) to capture the contribution of TM surface waves. Applying the modified Prony technique into this very large range lead to inaccuracy. As such, a two-level DCIM is employed. Two ranges of $t_1=[0,90]$ and $t_2=[90,120]$ are considered for TM reflection with parameters: $N_1^{TM}=22,\ N_2^{TM}=20,\ P_1^{TM}=12,\ P_2^{TM}=5$, while for TE reflection one-level DCIM with parameters: $T=8,\ N_{TE}=22,\ P_{TE}=12$ is adopted. Figure S5 compares the results of extrapolated and exact reflection coefficient for both polarizations. As it can be seen, the reflection coefficients are approximated with a high accuracy with this scheme.

Once the problem is solved and the dipole moments are obtained, one can repeat the same procedure for the transmission coefficients to obtain the transmitted field into other regions by evaluating the corresponding Sommerfeld integrals [5, 6].

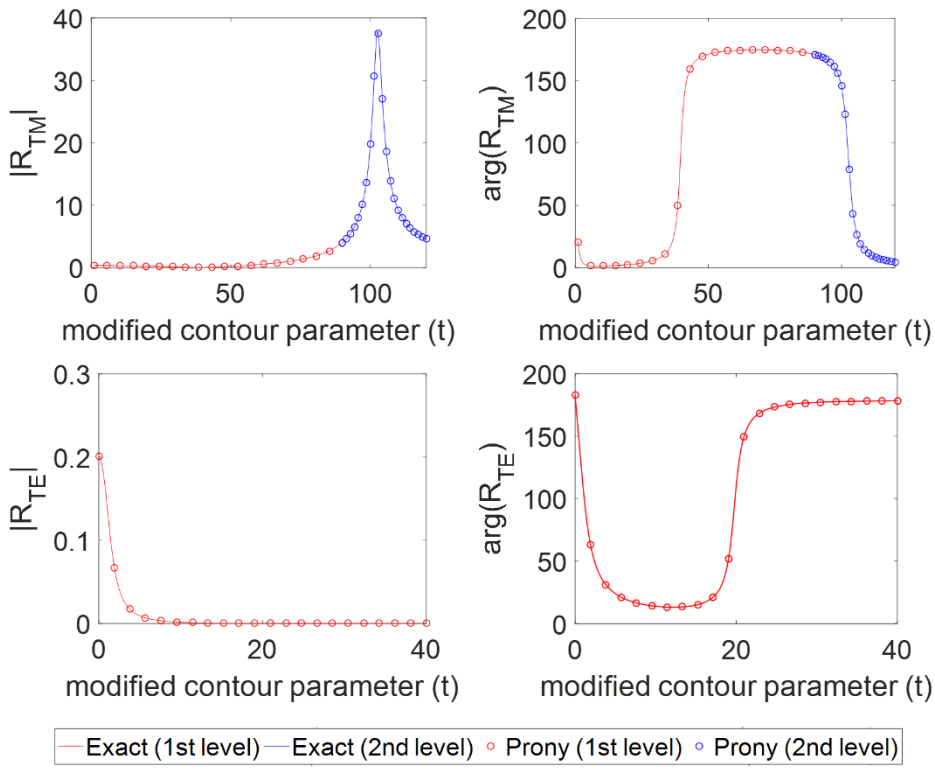

Figure S5. Comparison the exact and extrapolated reflection coefficient magnitude and phase for both TE and TM polarizations, corresponding to a Graphene placed onto a silica substrate. Two ranges of $t_1 = [0,90]$ and $t_2 = [90,120]$ are considered for TM reflection with parameters: $N_1^{TM} = 22,\ N_2^{TM} = 20,\ P_1^{TM} = 12,\ P_2^{TM} = 5$, while for TE reflection one-level DCIM with parameters: $T = 8,\ N_{TE} = 22,\ P_{TE} = 12$ is adopted.

4- Hierarchical Matrix (H-matrix):

Recently, several acceleration methods such as fast multipole-based methods, fast-Fourier transform (FFT)-based methods and fast low-rank compression methods have been proposed which can drastically reduce the computation complexity and memory requirements to the order of $O(N_{it} N \log(N))$. In this context, 3D-FFT [12, 13] and $\mathcal{H}$-matrix [14] have been previously implemented into the formulation of DDA. These techniques are often applied to the problems with free-space Green's function which requires discretization of the substrate. Special care and modifications has to be practiced for incorporation of layered media Green's function. For example, in [13] Yurkin and Huntermann modified and implemented 3D-FFT technique in DDA for particles near a plane interface by decomposing the layered media Green's functions into the terms with discrete convolution and correlation forms.

The $\mathcal{H}$-matrix provides a general mathematical framework [14-17] for low rank representation of interaction matrix, consisting of a collection of block matrices of various sizes. This results into compressed storage and reduces the computational complexity of matrix-vector multiplications which are the bottleneck of iterative solvers.

In the $\mathcal{H}$-matrix approach, first the structure is partitioned into subdomains by adopting a clustering scheme. An admissibility condition is employed to identify admissible subdomain pairs [15]:

$$\min\{\mathrm{diam}(X),\mathrm{diam}(Y)\} < \eta\,\mathrm{dist}(X,Y) \tag{S37}$$

where $\mathrm{diam}(X)$ denotes the maximal extent of subdomain X, $\mathrm{dist}(X,Y)$ is the minimal distance between subdomains X and Y and η is a positive parameter that can be used to control the admissibility condition. This condition ensures that the subdomains are geometrically well-separated as shown in Fig. S6.

The partitioning procedure is recursively applied to each subdomain until a prescribed number of iterations p is reached which is a parameter to control the clustering depth. This leads to hierarchy of blocks in the interaction matrix representing interactions between pairs of subdomains. The hierarchical block structure and the number of admissible blocks is dependent upon the geometry, clustering approach, clustering depth (p) and admissibility condition parameter η. A good clustering approach should make blocks become admissible as soon as possible. Several clustering approaches are available in order to obtain an optimum cluster tree such as nested dissection [18], cardinality balanced clustering [19], etc. In this work, a bounding box clustering is employed for the sake of simplicity [20]. A separation plane orthogonal to the x-axis is drawn through the center of the structure, dividing it into two –more or less equal- subdomains.

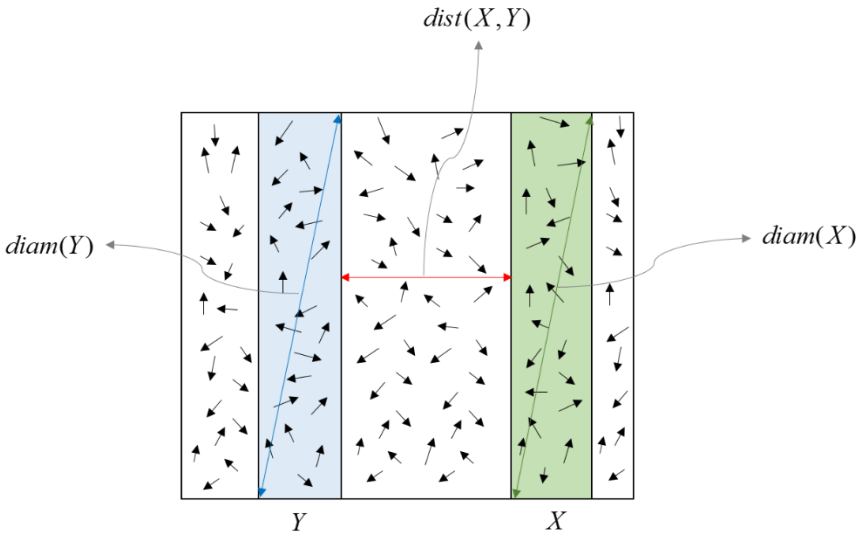

Figure S6. The schematic representation of geometric admissibility condition.

Having identified the admissible and inadmissible subdomain pairs, we can then approximate the interaction matrix $\hat{G}$ by its hierarchical representation $\hat{G}_H$. In this representation, the corresponding block matrices to inadmissible subdomain pairs (X,Y) not satisfying the criterion (S37), are computed exactly. While for admissible subdomain pairs (X,Y), the corresponding block matrices $\hat{G}_{(X,Y)} \in \mathbb{C}^{m\times n}$ are rank deficient and can be approximated by low rank

approximations (m and n denote the number of degrees of freedom in subdomains X and Y, respectively). The block matrix $\hat{G}_{(X,Y)} \in \mathbb{C}^{m\times n}$ is approximated by $\tilde{\tilde{G}}_{(X,Y)} \in \mathbb{C}^{m\times n}$ such as [17]:

$$\hat{G}_{(X,Y)} \simeq \tilde{\tilde{G}}_{(X,Y)} = \left(\hat{V}_{G_{(X,Y)}}\right)\left(\hat{W}_{G_{(X,Y)}}\right)^{*} \tag{S38}$$

with $\hat{V}_{G_{(X,Y)}} \in \mathbb{C}^{m\times k}$ and $\hat{W}_{G_{(X,Y)}} \in \mathbb{C}^{n\times k}$ and * standing for the complex conjugate. k is the rank of the representation. For $k(m+n) < mn$, $\tilde{\tilde{G}}_{(X,Y)}$ is called a low rank approximation of $\hat{G}_{(X,Y)}$, as the memory storage is reduced from $O(mn)$ to $O(k(m+n))$ by storing $\hat{V}_{G_{(X,Y)}}$ and $\hat{W}_{G_{(X,Y)}}$ instead of $\hat{G}_{(X,Y)}$ which is linear in m and n. The rank k dictates the compression rate and is the determined through a rank-revealing method such that the approximation of $\tilde{\tilde{G}}_{(X,Y)}$ in (S38) is accurate up to a prescribed relative accuracy ε.

In the low frequency regime where the domain of interest is electrically small, a constant rank can be used for low-rank representations without affecting the accuracy [15]. In this work, we have attempted to use H-matrix in dipolar equations for both individual element and array scale incorporating layered media Green's function. While the single element is subjected to the low frequency condition, the array scale analysis with layered media Green's function cannot be carried out with a constant rank as the contributions of guided modes and lateral waves from the substrate and the domain electrical size significantly affect the rank deficiency of the blocks and requires an adaptive rank revealing algorithm for a prescribed accuracy. Here, we use the partially pivoted adaptive cross approximation (ACA) algorithm [21-23] to compute the matrices $\hat{V}_{G_{(X,Y)}}$ and $\hat{W}_{G_{(X,Y)}}$ for the low rank approximation defined in (S38). ACA is a general adaptive algebraic approximation technique. A stopping criterion based on the relative error of the Frobenius norm in consecutive approximations $\dfrac{\left\|\tilde{\tilde{G}}_{(X,Y)}\right\|_F^{k+1} - \left\|\tilde{\tilde{G}}_{(X,Y)}\right\|_F^{k}}{\left\|\tilde{\tilde{G}}_{(X,Y)}\right\|_F^{k}}$ is used to avoid complete generation of $\hat{G}_{(X,Y)}$ [17]. The details of ACA can be found in [21-23] and are not repeated here. After assembly of each low rank representation through ACA, a recompression technique based on the singular value decomposition (SVD) is applied to reduce the rank even further [15, 17]. In this technique $\tilde{\tilde{G}}_{(X,Y)}$ is decomposed into a SVD-like decomposition $\tilde{\tilde{G}}_{(X,Y)} = \hat{Q}_V \hat{U}_R \hat{\sum} \left(\hat{Q}_W \hat{V}_R\right)^{*}$ by introducing QR-decompositions of $\hat{V}_{G_{(X,Y)}} = \hat{Q}_V \hat{R}_V$, $\hat{W}_{G_{(X,Y)}} = \hat{Q}_W \hat{R}_W$ and SVD of $\hat{R}_V \hat{R}_W^{*} = \hat{U}_R \hat{\sum} \hat{V}_R^{*}$. Then the singular values below the accuracy threshold and the corresponding singular vectors are discarded. The resultant rank will be minimal.

Once obtained the hierarchical representation of the interaction matrix, one has to solve the system of equations in which the interaction matrix is replaced by its hierarchical representation. For this purpose, iterative Krylov subspace methods such as generalized minimum residual (GMRES) and quasi minimal residual (QMR) can be employed. In this work the resulting set of $\mathscr{H}$-matrix equations are solved using generalized minimum residual (GMRES) [24] iterative algorithm without employing any preconditioning scheme. A threshold of 10^{-3} has been assigned in the ACA algorithm to obtain low rank approximations of the blocks corresponding to admissible cluster pairs, and a tolerance of 10^{-3} has been specified in the iterative GRMES solver.

The H-matrix with the adaptive rank revealing algorithm can be used in the dipolar equations for analysis of both single elements and embedded elements in the arrays with layered media Green's function. The computation complexity is highly dependent on the H-matrix partition. The bounding box clustering with a clustering depth of $p=5$ and admissibility condition parameter of $\eta=2$ results in a hierarchical block structure as shown in figure S7 for a V-shaped nanoantenna consisting of 8063 cells and a 2D array with 128×128 inclusions. The red blocks are corresponding to inadmissible pairs and are computed exactly while the green ones are pertaining to the admissible pairs and are stored in the low rank representation. As it can be seen, near diagonal blocks describing the self and near interactions are inadmissible and have the smallest size. For the V-shaped nanoantenna, the block structure exhibits a denser diagonal part corresponding to the part of the domain where the arms of the antenna are joint and a sparse part corresponding to the edges of the nanoantenna where the elements are far apart. While for the 2D array in a uniform grid, there is no diagonal inhomogeneity in the block structure. Each of the submatrices in the DDA interaction matrix, are partitioned as shown.

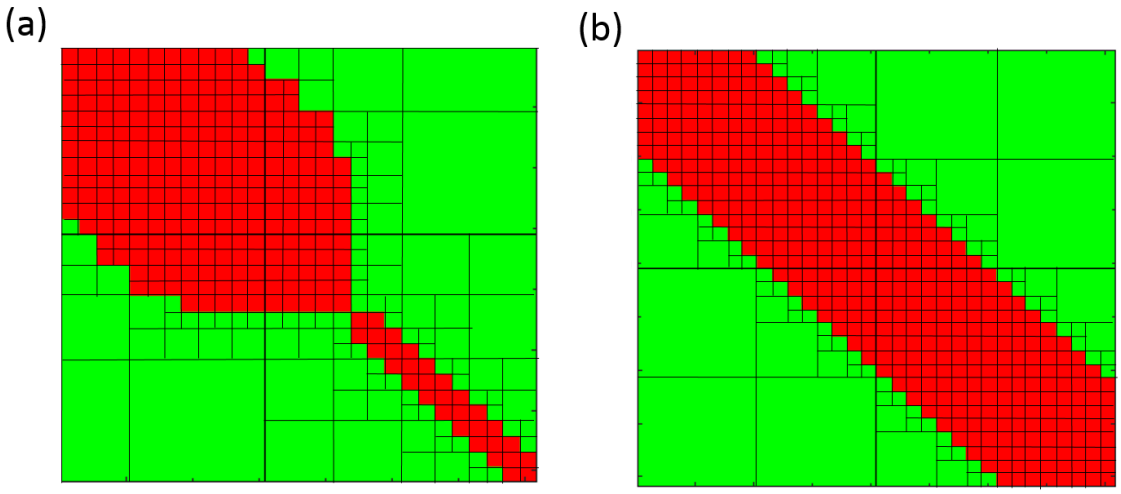

Figure S7. The hierarchical block structure resulted from a bounding box clustering with a clustering depth of p=5 and admissibility condition parameter of η=2 for (a) a V-shaped nanoantenna consisting of 8063 cells and (b) a 2D array with 128×128 inclusions.

5- Retrieved Polarizability Data of the Elements:

In this section, we provide the data for the retrieved polarizability tensors corresponding to the elements studied in the paper. The results can be used for homogenization of periodic metafilms [25] and model-order reduction in the analysis of aperiodic functional metasurfaces using dipolar equations as presented in this work. The polarizability tensor relates the local field at the phase center of dipoles to dipole moments as:

$$\begin{bmatrix} \overline{p} \\ \overline{m} \end{bmatrix} = \begin{bmatrix} \hat{\alpha}^{E} & \hat{\alpha}^{EH} \\ \hat{\alpha}^{HE} & \hat{\alpha}^{H} \end{bmatrix} \begin{bmatrix} \overline{E}^{loc} \\ \overline{H}^{loc} \end{bmatrix} \tag{S39}$$

In this work, we have used standing waves constructed by interference of plane waves, incident from opposing Cartesian directions as incident conditions. Six independent conditions are constructed by using the three Cartesian axes as incident directions, each with two orthogonal polarizations along the other two Cartesian axes [26]. As the linear superposition principle is rigorously satisfied in DDA, the choice of incidence conditions is immaterial for the final result.

We define:

$$\hat{\alpha} = \begin{bmatrix} \hat{\alpha}^{ee} & \hat{\alpha}^{em} \\ \hat{\alpha}^{me} & \hat{\alpha}^{mm} \end{bmatrix} = \begin{bmatrix} \hat{\alpha}^{E} / \varepsilon_0 & \hat{\alpha}^{EH} c \\ \hat{\alpha}^{HE} \eta_0 & \hat{\alpha}^{H} \end{bmatrix} \tag{S40}$$

where ε_0, c and η_0 are vacuum permittivity, speed of light in free space and free space impedance, respectively.

There are several constraints on $\hat{\alpha}$. In addition to the constraints imposed by the geometry of the scatterer, there are constraints due to reciprocity and to energy conservation. These constraints are described with Onsager relation which have been obtained for dynamic polarizability as [27]:

$$\left[\hat{\alpha}^{ee}\right] = \left[\hat{\alpha}^{ee}\right]^{\dagger}, \left[\hat{\alpha}^{mm}\right] = \left[\hat{\alpha}^{mm}\right]^{\dagger}, \left[\hat{\alpha}^{em}\right] = -\left[\hat{\alpha}^{me}\right]^{\dagger} \tag{S41}$$

where † stands for transpose.

Figure S8 demonstrates the magnitude and phase of all the polarizability tensor components for the plasmonics V-shaped nanoantenna units at $\lambda = 1.55\mu m$. All the other components not plotted here are less than 10^{-3} below the presented values and are negligible. The geometric parameters of the nanoantennas can be found in Table 1 in the manuscript. The transverse electric polarizability is the largest polarizability and thereby the V-shaped nanoantennas are strongly plasmonic. The normal electric polarizability α_{zz}^{ee} is very weak because the plasmonic elements are optically ultrathin. The off-diagonal elements of α^{ee} describe the rotational asymmetry of the nanoantennas. The magnetic polarizability components are all zero as the elements do not exhibit artificial magnetic response and there is only very small normal

component α_{zz}^{mm}. As the results indicate, the nanoantennas have bianisotropic nature as the off-diagonal elements α_{xz}^{em}, α_{yz}^{em}, α_{zx}^{em} and α_{zy}^{em} significantly exceed the magnetic polarizability. The obtained results are in a reasonable accordance with the results obtained in [26] for a similar element.

Once can notice that $\alpha_{xx}^{ee}=\alpha_{yy}^{ee}$, which is because of the symmetric configuration of nanoantennas with respect to x- and y- axis. Moreover, it can be clearly observed that $\left[\hat{\alpha}^{ee}\right]=\left[\hat{\alpha}^{ee}\right]^{\dagger}$, $\left[\hat{\alpha}^{mm}\right]=\left[\hat{\alpha}^{mm}\right]^{\dagger}$ and $\left[\hat{\alpha}^{em}\right]=-\left[\hat{\alpha}^{me}\right]^{\dagger}$ as the elements are reciprocal and must be in accordance with the Onsager-Casimir principle. This also verifies the accuracy of our retrieval scheme as all the constraints imposed by geometry and Onsager-Casimir principle are satisfied with a great accuracy.

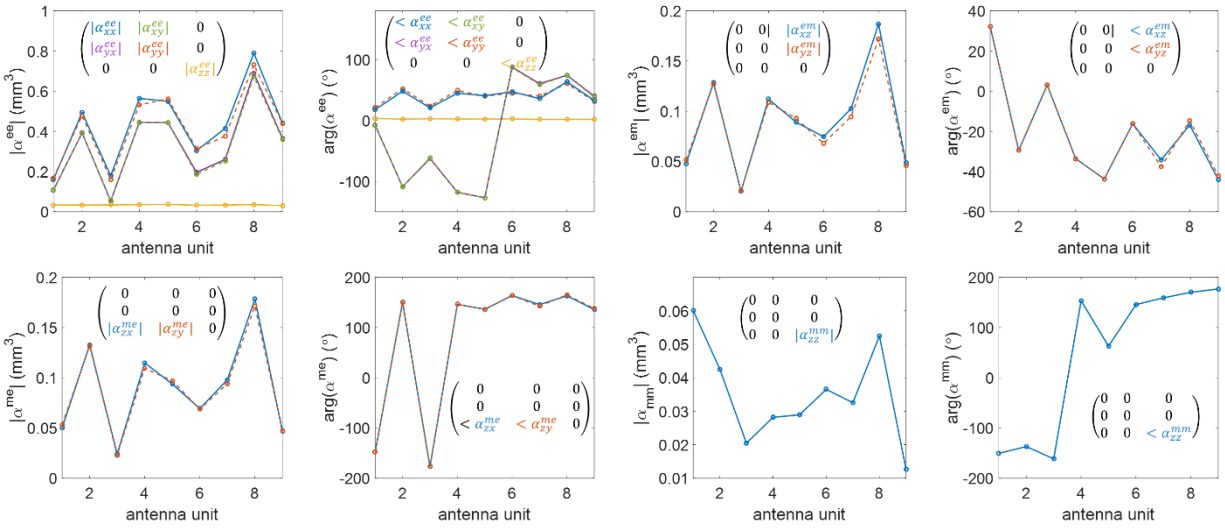

Figure S8. The retrieved polarizability tensor components corresponding to different V-shaped nanoantenna units with the geometric parameters given in Table 1 of the manuscript at $\lambda=1.55\mu m$.

The following plots demonstrate the magnitude and phase of all the polarizability tensors components for the silicon nanobars corresponding to the blue, green and red subcells of the multi-color hologram at the operating wavelengths of $\lambda_b=459nm$, $\lambda_g=512nm$ and $\lambda_r=650nm$. The components not plotted here are negligible. The geometric parameters of the nanoantennas are given in the manuscript. Unlike the plasmonic particles, high index dielectric nanoparticles can exhibit a strong magnetic response in the visible range. This can be seen from the results as the magnetic polarizability is comparable with the electric polarizability. Since the elements are completely achiral, the magneto-electric polarizability components are negligible. The off-diagonal transverse components $\alpha_{xy}^{ee,mm}$ and $\alpha_{yx}^{ee,mm}$ are zero only when rotation angle is $\theta=0^{\circ},90^{\circ},180^{\circ}$ where the nanobars are symmetric. The maximum cross-coupling occurs when the nanobars are tilted by $\theta=45^{\circ},135^{\circ}$. Unlike the optically ultrathin plasmonic elements, here the normal component of electric polarizability α_{zz}^{ee} is comparable to the transverse components

and is not negligible at all. One interesting feature that can be observed in all the elements is that the electric properties of the nanobars are mostly aligned with the longer axis and magnetic properties are mostly aligned with the shortest dimension. That explains the opposite trend in the variation of diagonal components of α^{ee} and α^{mm} versus rotation angle. As it is required by Onsager-Casimir principle, we must have: $\left[\hat{\alpha}^{ee}\right]=\left[\hat{\alpha}^{ee}\right]^{\dagger}$, $\left[\hat{\alpha}^{mm}\right]=\left[\hat{\alpha}^{mm}\right]^{\dagger}$. This condition is shown to be satisfied in the retrieved components with a great accuracy. Other constraints imposed by the geometry are: $\alpha_{xx,yy}(\theta)=\alpha_{xx,yy}(180^{\circ}-\theta)$, $\alpha_{xy}(\theta)=-\alpha_{xy}(180^{\circ}-\theta)$, $\alpha_{xx,yy}(\theta=0^{\circ})=\alpha_{yy,xx}(\theta=45^{\circ})$. All these conditions are satisfied in all the elements with a very high accuracy which verifies the validity of our retrieval scheme.

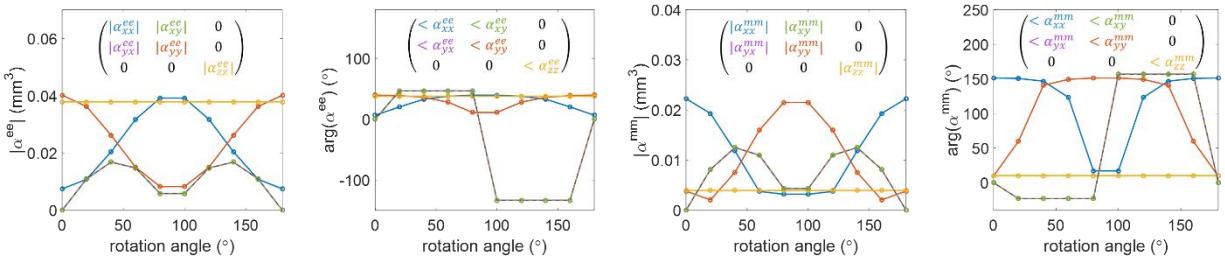

Figure S9. The retrieved polarizability tensor components corresponding to the silicon nanorod of blue subcell with the geometric parameters defined as *L*=125*nm*, *W*=35*nm*, *h*=120*nm* versus rotation angle at $\lambda_b=459nm$.

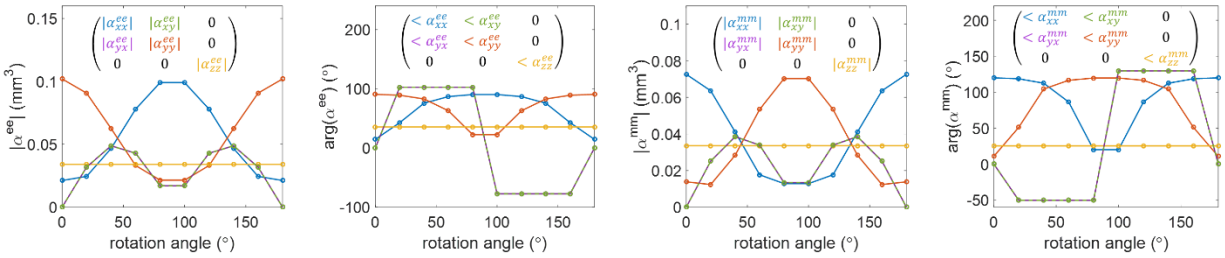

Figure S10. The retrieved polarizability tensor components corresponding to the silicon nanorod of blue subcell with the geometric parameters defined as *L*=250*nm*, *W*=60*nm*, *h*=80*nm* versus rotation angle at $\lambda_g=512nm$.

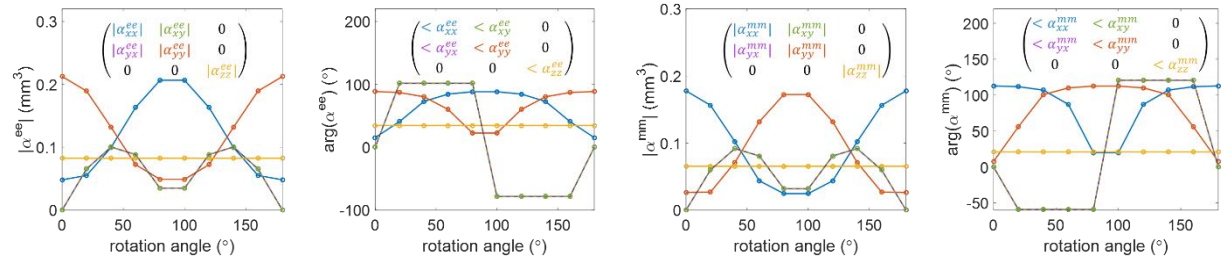

Figure S11. The retrieved polarizability tensor components corresponding to the silicon nanorod of the red subcell of hologram with the geometric parameters defined as *L*=335*nm*, *W*=80*nm*, *h*=120*nm* versus rotation angle at $\lambda_r=650nm$.

References:

[1] Campione, S.; Capolino, F. Ewald Method for 3D Periodic Dyadic Green's Functions and Complex Modes in Composite Materials Made of Spherical Particles Under the Dual Dipole Approximation. *Radio Sci.* 2012, *47*.

[2] Ewald, P. Die Berechnung Optischer Und Elektrostatischer Gitterpotentiale. *Ann. Phys.* 1921, *369*, 253-287.

[3] Jordan, K.; Richter, G.; Sheng, P. An Efficient Numerical Evaluation of the Green's Function for the Helmholtz Operator on Periodic Structures. *Journal of Computational Physics* 1986, *63*, 222-235.

[4] Valerio, G.; Baccarelli, P.; Burghignoli, P.; Galli, A. Comparative Analysis of Acceleration Techniques for 2-D and 3-D Green's Functions in Periodic Structures Along One and Two Directions. IEEE Transactions on Antennas and Propagation 2007, 55, 1630-1643.

[5] Chew, W. Waves and fields in inhomogeneous media; Van Nostrand Reinhold: New York, 1990.

[6] Tajdini, M.; Mosallaei, H. Characterization of Large Array of Plasmonic Nanoparticles On Layered Substrate: Dipole Mode Analysis Integrated with Complex Image Method. *Opt. Express* 2011, *19*, A173.

[7] Chen, Y.; Sha, W.; Choy, W.; Jiang, L.; Chew, W. Study on Spontaneous Emission in Complex Multilayered Plasmonic System via Surface Integral Equation Approach with Layered Medium Green'S Function. *Opt. Express* 2012, *20*, 20210.

[8] Kahn, M.; Mackisack, M.; Osborne, M.; Smyth, G. On The Consistency of Prony's Method and Related Algorithms. *Journal of Computational and Graphical Statistics* 1992, *1*, 329.

[9] Osborne, M.; Smyth, G. A Modified Prony Algorithm for Exponential Function Fitting. *SIAM J. Sci. Comput.* 1995, *16*, 119-138.

[10] Arand, B.; Hakkak, M.; Forooraghi, K.; Mohassel, J. Analysis of Aperture Antennas above Lossy Half-Space. *Progress in Electromagnetics Research* 2004, *44*, 39-55.

[11] Aksun, M. A Robust Approach for the Derivation of Closed-Form Green's Functions. *IEEE Transactions on Microwave Theory and Techniques* 1996, *44*, 651-658.

[12] Goodman, J. J.; Draine, B. T.; Flatau, P. J. Application of FastFourier-Transform Techniques to the Discrete-Dipole Approximation. Opt. Lett. 1991, 16, 1198−1200.

[13] Yurkin, M.; Huntemann, M. Rigorous and Fast Discrete Dipole Approximation for Particles near a Plane Interface. J. Phys. Chem. C 2015, 119, 29088-29094.

[14] Ansari-Oghol-Beig, D.; Rostami, M.; Chernobrovkina, E.; Saikin, S.; Valleau, S.; Mosallaei, H.; Aspuru-Guzik, A. Parametric Hierarchical Matrix Approach for The Wideband Optical Response of Large-Scale Molecular Aggregates. J. Appl. Phys. 2013, 114, 164315.

[15] Hackbusch, W. A Sparse Matrix Arithmetic Based On H -Matrices. Part I: Introduction to H-Matrices. Computing 1999, 62, 89-108.

[16] Wenwen, Chai.; Dan, Jiao. An H-Matrix-Based Integral-Equation Solver of Reduced Complexity and Controlled Accuracy for Solving Electrodynamic Problems. IEEE Trans. Antennas Propagat. 2009, 57, 3147-3159.

[17] Coulier, P.; François, S.; Lombaert, G.; Degrande, G. Application of Hierarchical Matrices to Boundary Element Methods for Elastodynamics Based On Green's Functions for a Horizontally Layered Halfspace. Engineering Analysis with Boundary Elements 2013, 37, 1745-1758.

[18] George, A. Nested Dissection of a Regular Finite Element Mesh. SIAM Journal on Numerical Analysis 1973, 10, 345-363.

[19] Bebendorf M. Hierarchical matrices: a means to efficiently solve elliptic boundary value problems. 1st ed.Springer Publishing Company; 2008.

[20] Börm, S.; Grasedyck, L.; Hackbusch, W. Introduction to Hierarchical Matrices with Applications. Engineering Analysis with Boundary Elements 2003, 27, 405-422.

[21] Bebendorf, M.; Rjasanow, S. Adaptive Low-Rank Approximation of Collocation Matrices. Computing 2003, 70, 1-24.

[22] Zhao, K.; Vouvakis, M.; Lee, J. The Adaptive Cross Approximation Algorithm for Accelerated Method of Moments Computations of EMC Problems. *IEEE Transactions on Electromagnetic Compatibility* 2005, *47*, 763-773.

[23] S. Borm, L. Grasedyck, and W. Hackbusch, "Hierarchical matrices," Lecture note 21 of the Max Planck Institute for Mathematics in the Sciences, 2003.

[24] Saad, Y.; Schultz, M. GMRES: A Generalized Minimal Residual Algorithm for Solving Nonsymmetric Linear Systems. *SIAM Journal on Scientific and Statistical Computing* 1986, *7*, 856-869.

[25] Simovski, C. On Electromagnetic Characterization and Homogenization of Nanostructured Metamaterials. *Journal of Optics* 2010, *13*, 013001.

[26] Arango, F.; Femius Koenderink, A. Polarizability Tensor Retrieval for Magnetic and Plasmonic Antenna Design. New Journal of Physics 2013, 15, 073023.

[27] Sersic, I.; Tuambilangana, C.; Kampfrath, T.; Koenderink, A. Magnetoelectric Point Scattering Theory for Metamaterial Scatterers. *Phys. Rev. B* 2011, *83*.